



Time-delayed reservoir computing based on an optically pumped spin VCSEL for high-speed processing

Yigong Yang · Pei Zhou · Penghua Mu ·
Nianqiang Li

Received: 17 March 2021 / Accepted: 7 December 2021 / Published online: 25 January 2022
© The Author(s), under exclusive licence to Springer Nature B.V. 2021

Abstract We report on the first numerical implementation of photonic reservoir computing (RC) based on an optically pumped spin vertical-cavity surface-emitting laser (spin VCSEL) with optical feedback and injection. The proposed RC aims at both fast, single task processing and parallel tasks processing, benefiting from feasible tunability and multiplexing of the left and right circularly polarized modes. We evaluate its prediction and classification abilities through two benchmarks, i.e., a Santa Fe time series prediction task and a waveform recognition task. In particular, both the influence of external and internal parameters on the prediction and classification performance is systematically analyzed. The numerical results show that the proposed RC based on a spin VCSEL has remarkable prediction and classification abilities over wider parameter ranges due to the feasible adjustment of the pump intensity and polarization as compared to conventional

VCSELs. Most importantly, because of its intrinsic fast response, the spin VCSEL-based RC system is capable of enhancing the information processing rate by significantly reducing the allowable feedback delay time and virtual node interval, reaching 20 Gbps for single task processing and 10 Gbps for parallel tasks processing, respectively. Such a spin VCSEL-based RC system has a potential to achieve high-speed information processing and lower power consumption.

Keywords Reservoir computing · Spin vertical-cavity surface-emitting lasers · Delay systems · Polarization dynamics

1 Introduction

To efficiently process the unprecedented amount of data at high speed, a variety of novel computational systems have been proposed. Among them, artificial neural networks (ANNs), which mimic the information processing way in the biological brain, have been successfully applied to tackle numerous necessary tasks with the improvement of machine learning. Generally speaking, ANNs have a powerful processing capability thanks to their trained connection weights and non-linear relationship between the input and output [1–3]. Although ANNs require complex training algorithms to learn the weights, they still penetrate into all aspects of technology and are widely studied. Later, recurrent neural networks (RNNs) are derived from

Y. Yang · P. Zhou · N. Li (✉)
School of Optoelectronic Science and Engineering &
Collaborative Innovation Center of Suzhou Nano Science
and Technology, Suzhou 215006, China
e-mail: wan_103301@163.com

Y. Yang · P. Zhou · N. Li
Key Lab of Advanced Optical Manufacturing Technologies
of Jiangsu Province & Key Lab of Modern Optical
Technologies of Education Ministry of China, Soochow
University, Suzhou 215006, China

P. Mu
Institute of Science and Technology for Opto-Electronic
Information, Yantai University, Yantai 264005, China

feed-forward neural networks and characterized by the existence of self-feedback nodes, so they are competent to process time-dependent series [4], which is a great advance compared to other ANNs. However, RNNs inevitably increase the complexity of the training procedure due to the self-feedback, where the connections in the network need training as well. Thus, a neuron-like computing system with a simple learning algorithm and small calculation power is highly desirable.

In 2007, the concept of reservoir computing (RC) was proposed by Verstraeten et al. [5] as a joint name of the echo state network (ESN) [6] and liquid state machine (LSM) [7]. The RC is composed of an input layer, a reservoir (usually consisting of a large number of physical nodes), and an output layer. It optimizes the traditional RNNs by fixed randomly connections both in the reservoir and between the input layer and the reservoir. To be precise, the portion in the RC needs to be trained is the output weight, consequently leading to simple training mechanism and low consumption. According to the literature, such RC has accomplished a large range of hard tasks with high performances, including chaos time series prediction, nonlinear channel equalization, hand written digit recognition, speech recognition [5–11], and so on.

In 2011, to avoid the large number of physical nodes and further simplify the RC architecture, time-delayed RC consisting of a nonlinear node with a delay feedback loop was proposed [12], which has attracted extensive interest in recent years [13–29]. Especially, the time-delayed RC schemes based on semiconductor lasers (SLs) have been vastly investigated due to their fast response and low energy consumption features [11]. Since Brunner et al. proposed a time-delayed RC system in 2013 based on transient responses of a SL with delayed feedback for the first time [13], both the performance and the information processing rate became the focus of the laser-based RC. For example, Nakayama et al. adopted chaos mask to achieve better prediction performance compared to other masks, and confirmed by a chaotic time series prediction task numerically [14] as well as experimentally [15]. In 2018, Nguimdo et al. [16] numerically investigated the prediction and reconstruction abilities of the time-delayed RC based on a single quantum cascade laser (QCL) with optical feedback. The results of performing different tasks show robustness for feedback phase. In the same year, time-delayed RC formed

by a SL subject to double optical feedback and injection was proposed, which realized a prediction error below 0.03 at the processing rate of 1 Gbps [17]. In 2020, Guo et al. improved the information processing rate to 10 Gbps through a compact semiconductor nanolaser with optical feedback under electrical modulation [18]. Furthermore, the SL-based RC allowing for simultaneously accomplishing several different tasks has already entered people's vision. For example, Nguimdo et al. [19, 20] demonstrated a parallel processing time-delayed RC system based on a semiconductor ring laser (SRL) subject to optical feedback, which can simultaneously process the nonlinear channel equalization task and time series prediction task by multiplexing the clockwise and counterclockwise modes of the SRL. However, this system exhibited a low processing speed of 0.25 Gbps and a degraded performance due to the unwanted coupling effects between the directional modes. Interestingly, vertical-cavity surface-emitting lasers (VCSELs) with rich polarization dynamics and low power consumption were proposed to improve the computational accuracy and the processing rate by Vatin et al. [21, 22]. Furthermore, Guo et al. proposed a four-channel RC system based on two mutually coupled VCSELs by taking advantage of the orthogonal polarization modes and numerically demonstrated its high computing efficiency [23]. The more exciting thing is that an ultrafast processing rate of 20 Gbps was realized in total four polarization modes of the two VCSELs. More recently, it has been demonstrated numerically [24] and experimentally [25] that even a single conventional VCSEL allows for the parallel processing by making use of the polarization multiplexing technology.

The above VCSEL-based RC shows a remarkable computing performance largely benefited from the multiplexing of the two linear polarization modes, and therefore has a susceptibility to the stability of modes. The two orthogonal polarization modes of conventional VCSELs are usually inadequately stable, and in other words, polarization switching occurs as the operation condition varies. These phenomena definitely degrade the computing performance. On the contrary, spin VCSELs, whose emitted polarization can be readily controlled via the pumping either electrical or optical, can exhibit superior properties over conventional VCSEL counterparts, including precise spin control of the lasing output, threshold reduction, and much faster dynamics [30–33]. In our previous works, the

dynamics of solitary spin VCSELs including steady-state operation, polarization oscillations, and rich bifurcations, and its potential application to secure communications have been well studied [35–42]. If such novel spin VCSELs are applied to RC, several features might be outlined as follows. Firstly, the complicated dynamics can be found in a spin-VCSEL without feedback [37], which may enrich the virtual node states and contribute to improving RC performance. Secondly, the spin VCSEL allows fast polarization dynamics of the order of the magnitude of ~ 200 GHz or even higher [34], which may enhance the computing rate. Thirdly, due to its threshold reduction [33], lower power consumption might be expected in the practical application. Compared with electrical spin-injection, optical pumping can generate spin-oriented carriers without the limitation of magnetic fields and temperatures [43]. On the other hand, Nguimdo et al. have demonstrated that an optically pumped erbium-doped microchip laser can be used to implement a RC system [26], which yields prediction performance comparable to those obtained for electrically pumped lasers. Hence the optically pumped spin VCSEL is a potential candidate to realize time-delayed RC with enhanced computing performance.

In this work, a time-delayed RC system based on an optically pumped spin VCSEL subject to optical feedback and injection is proposed to realize high-speed single task or parallel tasks processing. We will demonstrate how fast dynamics properties allowed by the spin VCSEL can be beneficially employed for high-speed processing. Here, both the left circularly polarized (LCP) and right circularly polarized (RCP) modes in the spin VCSEL are adopted to build the reservoir. The consistent or independent input signals correspond to the case of single task or two different tasks processing, respectively. The parameter region for good computing performance is numerically explored. Besides, we also investigate the influence of some important external and internal parameters on the prediction and classification abilities of the spin VCSEL-based RC, to show the robustness of the proposed scheme. This paper is organized as follows. In Sect. 2, the conceptual scheme of the RC system and the theoretical model of an optically pumped spin VCSEL with optical feedback and injection are described. Section 3 provides the main numerical results for spin VCSEL-based RC for single task and parallel tasks processing, where a large range of parameter dependence is

also explored. Finally, our basic conclusion is given in Sect. 4.

2 Theory and model

The conceptual scheme of the proposed RC based on an optically pumped spin VCSEL subject to optical feedback and injection is shown in Fig. 1, which is divided into three parts: an input layer, a reservoir and an output layer. The input layer is primarily composed of two drive SLs (SL1 and SL2), two Mach-Zehnder modulations (MZM1 and MZM2) and two polarization controllers (PC1 and PC2). Signals $u_{\pm}(n)$ are pre-processed with two random masks, which are used to construct two masked input signal $S_{\pm}(t)$, and are, respectively, injected into the RCP and LCP modes of the spin VCSEL through external modulation. The masks have discrete $\{-1, 1\}$ values that vary at each interval θ in a period of T and can ensure the variability of masked signals. The PC1 and PC2 are used to shift the polarization states of two drive lasers. The LCP and RCP modes of the optically pumped spin VCSEL with a feedback loop can present abundant nonlinear responses, thereby form the reservoir. The feedback delay time τ is determined by the length of delay line. The variable optical attenuator is adopted to control the feedback strength while the circulator is used to ensure the light transmission direction. As for the output layer, the virtual nodes are sampled from the two polarization modes at a fixed interval θ during each feedback time $\tau = T$, leading to $M = \tau/\theta$ node states in both two modes. For single task processing, we use consistent series as $u_{+}(n)$ and $u_{-}(n)$ in the input layer and compute the results using all $2M$ virtual nodes. When dealing with two independent tasks, disparate signals are chosen and output results are determined by the independent linear combination of the virtual nodes from the two polarization modes and the corresponding output weights. The ridge regression method is used in our system to minimize the mean-square error between target and output values.

The spin-flip model (SFM) is used to model the optically pumped spin VCSEL with optical feedback and injection. In this model, the influence of the spontaneous emission noise on the laser mode is considered using the spontaneous factor β and the noise source ξ , which is the independent Gaussian white noise with unit variance and zero mean. The complex electric field

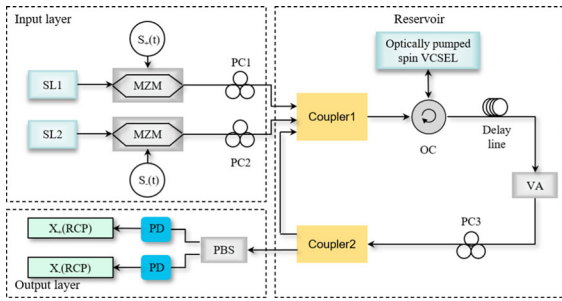


Fig. 1 System diagram of the RC based on an optically pumped spin VCSEL. SL, semiconductor laser; MZM, Mach-Zehnder modulator; PC, polarization controller; VA, variable optical attenuator; OC, optical circulator; PBS, polarization beam splitter; PD, photodiode

E , the difference between carrier inversions m and the total carrier population N can be modeled by the following rate equations [44, 45]:

$$\frac{dE_{\pm}}{dt} = \kappa(1 + i\alpha)(N \pm m - 1) - (\gamma_a + i\gamma_p)E_{\mp} + k_f E_{\pm}(t - \tau)e^{-i\omega_0\tau} + k_{inj} E_{inj\pm} + \xi_{\pm} \sqrt{\beta\gamma(N \pm m)} \quad (1)$$

$$\frac{dN}{dt} = \gamma[\eta_+ + \eta_- - (1 + |E_+|^2 + |E_-|^2)N - (|E_+|^2 - |E_-|^2)m] \quad (2)$$

$$\frac{dm}{dt} = \gamma(\eta_+ - \eta_-) - [\gamma_s + \gamma(|E_+|^2 + |E_-|^2)]m - \gamma(|E_+|^2 - |E_-|^2)N \quad (3)$$

where the subscripts $+, -$ indicate the RCP and LCP modes, respectively. Other parameters are defined as follows: γ_a represents the linear dichroism, γ_p is the linear birefringence, κ is the optical field decay rate, γ is the decay rate of N , γ_s is the spin-flip relaxation rate, and α is the linewidth enhancement factor. The experimentally available parameter $\eta = \eta_+ + \eta_-$ is the total normalized pump power of the optical pumping and $P = (\eta_+ - \eta_-)/(\eta_+ + \eta_-)$ is defined as the pump polarization ellipticity, where η_+ and η_- are dimensionless circularly polarized pump components that describe the polarized optical pumping.

The third term on the right-hand side of Eq. (1) is the feedback term, where k_f is the feedback strength, τ is the feedback delay time, and ω_0 is the optical angular frequency, respectively. The fourth term on the right-hand side of Eq. (1) describes the optical injection

effect, where the k_{inj} stands for the injection strength, and $E_{inj\pm}$ represent the outputs of the two MZMs described as [29]:

$$E_{inj\pm} = \frac{|E_0|}{2} \{1 + e^{i[S_{\pm}(t) + \Phi_0]}\} e^{i\Delta\omega_{inj\pm}t} \quad (4)$$

In Eq. (4), the E_0 denotes the injection field amplitude from the drive laser, and the masked input signals $S_{\pm}(t)$ are generated by multiplying the input data $u_{\pm}(n)$ and the mask signals $M_{\pm}(t)$, i.e., $S_{\pm}(t) = u_{\pm}(n) \times M_{\pm}(t)$. Φ_0 is the normalized bias voltage of MZMs. $\Delta\omega_{inj\pm}$ are the angular frequency detuning between the laser fields E_{\pm} and the external injection fields $E_{inj\pm}$, which can be calculated from the corresponding optical frequency detuning Δf as $\Delta\omega_{inj\pm} = 2\pi\Delta f$.

In order to investigate the performance of the RC system based on an optically pumped spin VCSEL, we use two classical benchmark tasks, i.e., a Santa Fe time series prediction task and a waveform recognition task. The first task aims to perform single-point prediction of the Santa-Fe chaotic time series experimentally recorded from a chaotic far-infrared laser [46]. We select 3000 and 1000 points from the chaotic data for training and testing, respectively. For the waveform recognition task, a sequence of random input data consists of square, sine and triangle waves (each of them is discretized into 10 points per period). Total 4000 points are used to realize the classification (likewise, 3000 for training and 1000 for testing), with the target value 0 for square wave, 1 for sine wave, and 2 for triangle wave [24]. For both tasks, the normalized mean square error (NMSE) between the target value y and the predicted value Y is calculated as an indicator for the performance of the RC scheme [29]:

$$NMSE = \frac{1}{L} \frac{\sum_i^L (y(i) - Y(i))^2}{\sigma^2} \quad (5)$$

where L is the number of the test data, n is the discrete time index, and σ denotes the standard deviation of the target value y . The lower NMSE value means better performance, and more concretely, the performance can be considered good enough when NMSE is less than 0.1. In the following section, the mean and the standard deviation of the NMSE values for 5 runs are shown except Figs. 2 and 9, where the vertical bar depicts the standard deviation.

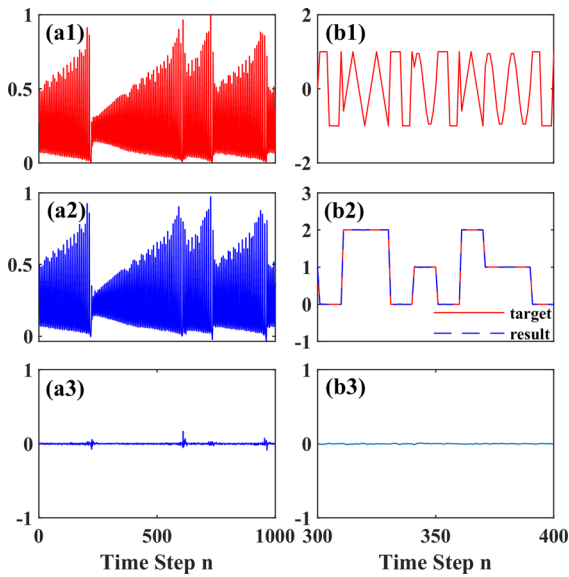


Fig. 2 Performance illustration of **a** the time series prediction task and **b** the waveform recognition task with $k_f = 30 \text{ ns}^{-1}$, $k_{inj} = 60 \text{ ns}^{-1}$, and $\Delta f = -20 \text{ GHz}$. **a1** temporal waveform of the original signal, **a2** predicted waveform by the proposed RC, and **a3** the error signal between the original signal and the predicted signal. **b1** temporal waveform of the random input wave, **b2** comparison between the classification target and result, and **b3** the error between the original waveform and the predicted waveform

3 Numerical results

In this section, we use the above-mentioned benchmark tasks to evaluate the performance of our proposed RC system both for processing a single task and two independent tasks in parallel. In our numerical simulation, the fourth-order Runge–Kutta algorithm is employed to solve Eqs. (1)–(3), and the following parameter values that make the spin VCSEL yields a steady-state output when absent from the modulated input data are chosen [37]: $\kappa = 230 \text{ ns}^{-1}$, $\alpha = 4$, $\gamma_s = 30 \text{ ns}^{-1}$, $\gamma_a = 0 \text{ ns}^{-1}$, $\gamma_p = 8.8 \text{ ns}^{-1}$, $\gamma = 0.68 \text{ ns}^{-1}$, $P = 0.1$, $\eta = 1.5$, $k_f = 30 \text{ ns}^{-1}$, $\tau = 1 \text{ ns}$, $\Phi_0 = 0$, $k_{inj} = 60 \text{ ns}^{-1}$, $\Delta f = -20 \text{ GHz}$, $E_0 = 1.5$, and $\beta = 10^{-6}$. For the reservoir, a virtual node interval of $\theta = 10 \text{ ps}$ is used. It should be noted that the above parameter values are kept constant, unless otherwise specified.

3.1 Single task processing

Firstly, to realize the single task processing, both the RCP and LCP are utilized to execute a specific bench-

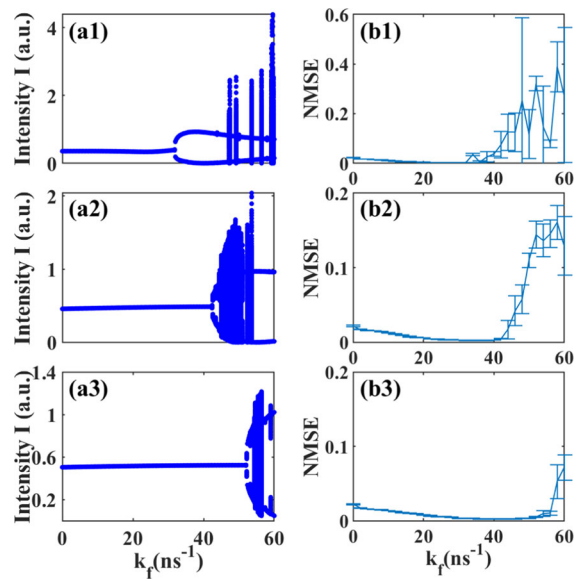


Fig. 3 **a** Bifurcation diagrams and **b** NMSE values of the RC system as a function of the feedback strength k_f with $\Delta f = -20 \text{ GHz}$. (a1, b1) $k_{inj} = 20 \text{ ns}^{-1}$, (a2, b2) $k_{inj} = 40 \text{ ns}^{-1}$, and (a3, b3) $k_{inj} = 60 \text{ ns}^{-1}$

mark task. To begin with, the target value and predicted value for the Santa Fe time series prediction task are shown in Fig. 2a1–a3. The NMSE value in this case is estimated as 0.0025, which means that our RC system has excellent prediction ability. In addition, the corresponding result for waveform recognition task can be found in Fig. 2b1–b3, with a NMSE value as low as 3.02×10^{-5} . For both tasks, the prediction results can almost overlap with the targets, as shown in Fig. 2a3 and b3, where the error is negligible. This indicates that outstanding performance can be expected for the two tasks in the proposed RC. For simplicity, we only focus on the Santa Fe time series prediction task for single task processing because of the consistent trends of the two tasks.

It is well-accepted that the optimal performance of the time-delayed RC largely benefits from the stable steady state of the used laser [12]. Therefore, it is of vital importance to investigate the relationship between the injection locking area and the prediction performance of the current RC. To this end, one-parameter bifurcation diagrams representing the intensity extrema (the bifurcation can also be solved by other mathematical tools [48]) as a function of the feedback strength k_f are depicted in Fig. 3a1–a3, where the input masked signal $S_{\pm}(t)$ is set to 0. It is worth noting that no noise

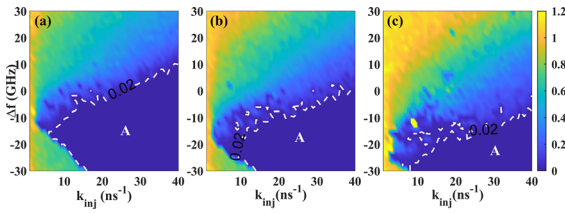


Fig. 4 Two dimensional maps of the NMSE in the plane of the injection strength k_{inj} and the frequency detuning Δf . **a** $k_f = 10 \text{ ns}^{-1}$, **b** $k_f = 20 \text{ ns}^{-1}$, and **c** $k_f = 30 \text{ ns}^{-1}$

is added to the model for better classification of the laser dynamics when drawing the bifurcation diagrams, i.e., $\beta = 0$. Accordingly, the NMSE as a function of the feedback strength k_f can be found from Fig. 3b1–b3. In Fig. 3, three levels of the injection strength k_{inj} are considered, and only the results computed from the RCP intensity are presented in Fig. 3a since the results for the RCP and LCP are almost identical. For an intermediate value of the injection strength $k_{inj} = 20 \text{ ns}^{-1}$, it can be observed from Fig. 3a1 that the stable steady state exists when k_f is less than 32 ns^{-1} . As the injection strength k_{inj} is increased gradually, we observe the stabilization of the laser dynamics in a wider range of k_f , as shown in Fig. 3a2 and (a3). This is expected since injection locking can be found in a wider area of parameters as stronger injection condition is applied for a given detuning frequency. According to Fig. 3b1–b3, good consistence between the NMSE values and bifurcation diagrams is confirmed. In all cases of k_{inj} , the NMSE curve decreases first, reaches a minimum, and finally increases dramatically as k_f is increased. It is interesting to find that the lowest NMSE is obtained before instability occurs in the spin VCSEL-based RC, consistent with the literature [12].

To further identify the influence of the optical injection on the prediction performance of the proposed RC, we turn to draw the two-dimensional maps of NMSE values in the plane of k_{inj} and Δf . Here, three values of the feedback strength, i.e., $k_f = 10, 20$ and 30 ns^{-1} are considered. The results are shown in Fig. 4, and in all panels, the parameter space of k_{inj} and Δf leading to better prediction performance with $\text{NMSE} \leq 0.02$ is denoted as A. As shown in Fig. 4a, the region A, resembling a “V” shape, is mainly located at negative Δf for $k_f = 10 \text{ ns}^{-1}$, and a wider region can be found for larger k_{inj} . Fig. 4b indicates that a larger value of the feedback strength, i.e., $k_f = 20 \text{ ns}^{-1}$, leads to a narrower region A and to the occurrence of a

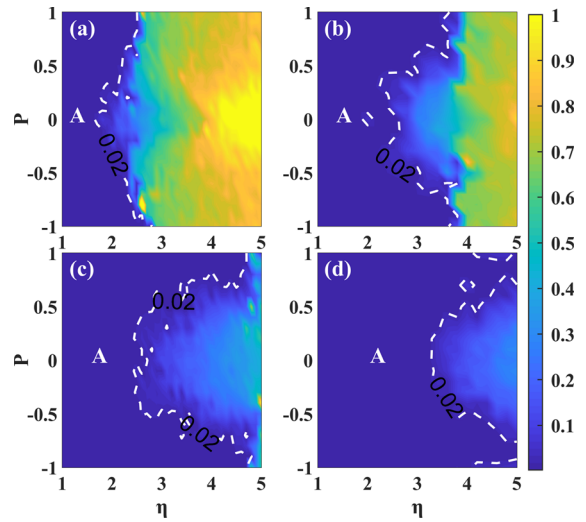


Fig. 5 Two dimensional maps of the NMSE in the plane of the pump polarization ellipticity P and the total normalized pump power η of the optical pumping with $k_f = 30 \text{ ns}^{-1}$ and $\Delta f = -20 \text{ GHz}$. **a** $k_{inj} = 20 \text{ ns}^{-1}$, **b** $k_{inj} = 30 \text{ ns}^{-1}$, **c** $k_{inj} = 40 \text{ ns}^{-1}$, and **d** $k_{inj} = 60 \text{ ns}^{-1}$

shift toward negative Δf . As the feedback strength is further increased to $k_f = 30 \text{ ns}^{-1}$, a more remarkable shifting can be observed in Fig. 4c, and in this case, only sufficiently negative Δf and intermediate to large k_{inj} can guarantee the good prediction performance. In fact, the good prediction region is almost in line with the injection lock area regardless of the feedback strength k_f . Therefore, detuning the response laser negatively with respect to the drive laser is beneficial for injection locking and thus for better prediction results.

For the specific spin VCSEL-based RC, there are other two experimentally available parameters, i.e., the pump polarization ellipticity P and the total normalized pump power of the optical pumping η , which are two key parameters modeling the external optical pumping. It is well examined that a spin VCSEL undergoes a variety of bifurcations and thus supports rich dynamics as either the P or η is varied [40]. Thus, it is interesting to study their influence on the performance of the RC. Here, for different k_{inj} , the two-dimensional maps of NMSE values in the parameter space of P and η are shown in Fig. 5. The region of lower NMSE values ($\text{NMSE} \leq 0.02$) is also termed A, which represents better prediction performance. Several important features can be identified from this figure. Firstly, the region A is symmetric with respect to the polarization ellipticity $P = 0$. This can be understood by the dynamics

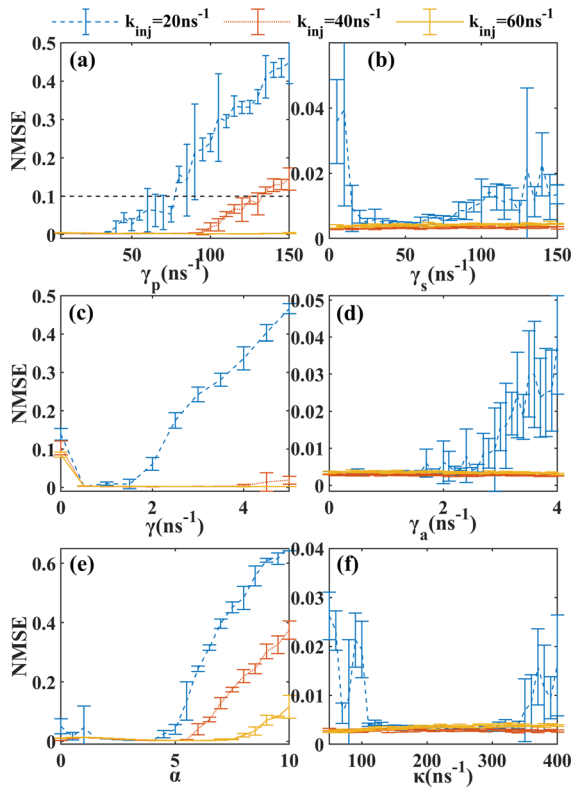


Fig. 6 The NMSE values as a function of the internal parameters with different values of $k_{inj} = 20, 40,$ and 60 ns^{-1} . **a** γ_p , **b** γ_s , **c** γ , **d** γ_a , **e** α , and **f** κ

of the spin VCSEL is symmetric for positive and negative values of the polarization ellipticity. Secondly, better prediction performance is always achieved for the low pump power η , which is similar to the case of the electrical pump. In that case, low prediction errors are obtained when the laser is biased close to the threshold. Thirdly, given the pump power η , larger absolute values of the polarization ellipticity leads to lower NMSE values, where one polarization mode is dominated. Finally, the region A expands in size as the injection strength k_{inj} increases. This is because that it is much easier to injection-lock the spin VCSEL for larger k_{inj} , no matter what the optical pumping condition is.

Subsequently, we evaluate the NMSE values as a function of some key internal parameters to give a thorough understanding of operating conditions of the proposed RC. The obtained results can be seen in Fig. 6. The above results have shown that the injection strength plays an important role in the prediction performance, so three injection levels, i.e., $k_{inj} = 20, 40, 60 \text{ ns}^{-1}$,

are adopted. According to Fig. 3, the feedback strength k_f is fixed at 30 ns^{-1} to ensure stable steady-state operation originally. We consider single parameter variation when other parameters are kept constant. Figure 6a illustrates the NMSE values as a function of the linear birefringence γ_p (can be controlled through mechanical strain). For $k_{inj} = 20 \text{ ns}^{-1}$ and $k_{inj} = 40 \text{ ns}^{-1}$, the NMSE values keep at the around of 0.01 before reaching a critical value of γ_p , and then significantly increases with the further increment of γ_p . In addition, a wider range of γ_p leading to good performance ($\text{NMSE} \leq 0.1$) is found for a larger value of k_{inj} . Especially in the case of $k_{inj} = 60 \text{ ns}^{-1}$, the discernible fluctuations of the NMSE values disappear and maintain an extremely low level. Figure 6b provides the NMSE curves versus spin-flip relaxation rate γ_s , which is material-dependent but can be changed via laser design. The obvious variation of the NMSE values is shown only for $k_{inj} = 20 \text{ ns}^{-1}$, whereas for $k_{inj} = 40 \text{ ns}^{-1}$ and $k_{inj} = 60 \text{ ns}^{-1}$, the performance of our RC system is hardly affected by γ_s . Besides, the effect of γ on the NMSE values is given in Fig. 6c. In the case of weak injection of $k_{inj} = 20 \text{ ns}^{-1}$, the trend of the NMSE variation firstly decreases, reaches its minimum, and then increases with the increase of γ . A larger injection strength, e.g., $k_{inj} = 40 \text{ ns}^{-1}$ and 60 ns^{-1} , can contribute to basically identical NMSE values under $0.5 \text{ ns}^{-1} \leq \gamma \leq 4 \text{ ns}^{-1}$. The similar stability for linear dichroism γ_a in Fig. 6d, while only the NMSE curve for $k_{inj} = 20 \text{ ns}^{-1}$ shows an upward trend as γ_a is increased. As shown in Fig. 6e, when the linewidth enhancement factor α is larger than a critical value and increases further, the prediction performance of the RC worsens. The stronger the injection strength is, the larger the critical α is. It can be seen that the critical values of α for three different injection conditions are 4, 5.5 and 7, respectively. Finally, in Fig. 6f, the values and fluctuations of the NMSE appear for $k_{inj} = 40 \text{ ns}^{-1}$ either when the optical field decay rate κ is too small or large. In contrast, no obvious changes can be identified as κ is varied for $k_{inj} = 20 \text{ ns}^{-1}$ and $k_{inj} = 60 \text{ ns}^{-1}$. Note that, on the one hand, the variations of γ_s , γ_a and κ does not force the NMSE values to be larger than the acceptable NMSE level, i.e., $\text{NMSE} \leq 0.1$, which means that good prediction performance is maintained as these parameters are varied. On the other hand, no matter which internal parameter we change, the larger injection always makes the RC system be easier to achieve low NMSE. That is to say,

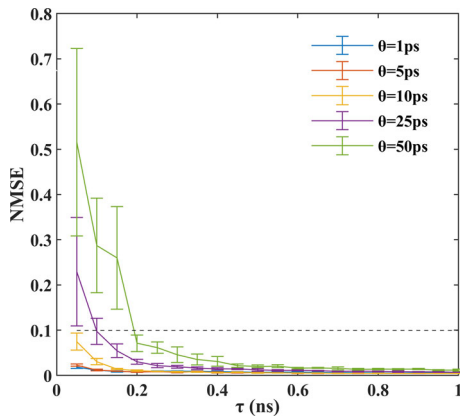


Fig. 7 The NMSE values as a function of the delay time τ with five different values of the virtual node interval, i.e., $\theta = 1, 5, 10, 25,$ and 50 ps

the robustness to the internal parameter fluctuation can be enhanced by increasing the injection strength k_{inj} . This also indicates that the proposed RC can achieve the good prediction in wide parameter space.

Fast information processing rate is one of the pursued goals in the RC field, and can be calculated as the reciprocal of the feedback delay time τ , i.e., $B = 1/\tau$. Moreover, the shorter delay line undoubtedly contributes to the miniaturization of time-delayed RC systems and their engineering application. Therefore, the influence of the delay time τ on the RC performance is discussed in Fig. 7. Based on the previous results, $k_{inj} = 60 \text{ ns}^{-1}$ and $k_f = 30 \text{ ns}^{-1}$ are adopted for achieving better prediction performance. As τ is decreased, the prediction performance becomes worse mainly because of the less available virtual nodes. In Fig. 7, various virtual node intervals θ are compared. It can be found that smaller θ can guarantee the enduring prediction error of our RC system. More precisely, in the three cases of $\theta \leq 10$ ps, the NMSE values are always lower than 0.1 even for an especially short delay time τ , i.e., $\tau = 0.05$ ns. These results demonstrate that the spin VCSEL-based RC system can process a single information computing task at the rate up to 20 Gbps. To gain further insight into the influence of τ and θ , Fig. 8 depicts the NMSE values as a function of the feedback strength k_f for $k_{inj} = 60 \text{ ns}^{-1}$. In this figure, various values of τ and θ are considered. As can be seen, for large delay times τ , e.g., $\tau = 1$ ns in Fig. 8a and $\tau = 0.4$ ns in Fig. 8b, the low prediction errors can be achieved in a wide range of k_f , regardless of θ .

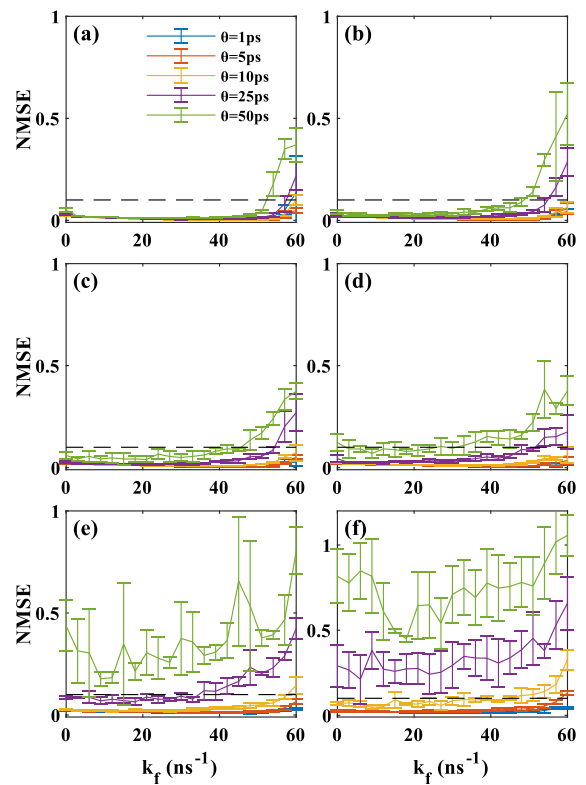


Fig. 8 The NMSE values as a function of the feedback strength k_f for **a** $\tau = 1$ ns, **b** $\tau = 0.4$ ns, **c** $\tau = 0.3$ ns, **d** $\tau = 0.2$ ns, **e** $\tau = 0.1$ ns and **f** $\tau = 0.05$ ns, and for five different values of the virtual node interval, i.e., $\theta = 1, 5, 10, 25,$ and 50 ps

As the delay time τ decreases to a critical value, e.g., $\tau = 0.3$ ns in Fig. 8c and $\tau = 0.2$ ns in Fig. 8d, the prediction errors gradually become sensitive to the choice of θ . When the delay time τ is too small, e.g., $\tau = 0.1$ ns in Fig. 8e and $\tau = 0.05$ ns in Fig. 8f, only extremely small values of θ can guarantee the satisfied RC performance, which also set higher demands for the data acquisition device.

3.2 Parallel tasks processing

In order to realize the parallel tasks processing, the RCP and LCP modes in the spin VCSEL-based RC system are utilized to deal with the time series prediction task (denoted as T-task) and the waveform recognition task (denoted as W-task), respectively. However, the reservoir is operating in the same condition as that in the case of single task processing. Typical computing results are shown in Fig. 9, from which one can see

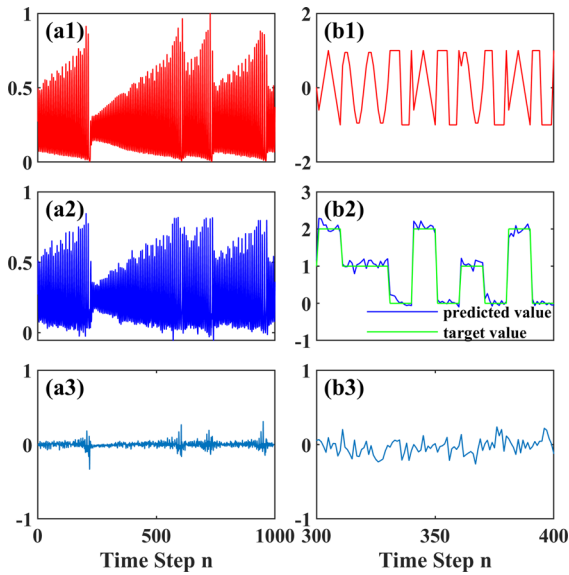


Fig. 9 Parallel processing performance illustration of **a** time series prediction task and **b** waveform recognition task with $k_f = 30 \text{ ns}^{-1}$, $k_{inj} = 60 \text{ ns}^{-1}$, $\Delta f = -20 \text{ GHz}$. **a1** temporal waveform of the Santa Fe data, **a2** Predicted waveform by the proposed RC, and **a3** the error signal between the original signal and the predicted signal. **b1** temporal waveform of the random input wave, **b2** comparison between the classification target and result, and **b3** the error signal between the original waveform and the predicted waveform

satisfactory prediction performance for parallel tasks processing. It is worth noting that the NMSE values of the time series prediction task and the waveform recognition task are estimated as 0.03478 and 0.03008, respectively, which is much larger than those for single task processing (Fig. 3). This is due to the fact that the inevitable coupling between two polarization modes leads to the degradation. In fact, this phenomenon has also been observed in the RC based on either semiconductor ring lasers [19] or conventional VCSELs [24], where there exist two modes.

Likewise, the influence of some external parameters on the RC computing performance is evaluated first. Fig. 10 illustrates the dependence of the prediction and classification performance on the feedback strength k_f for three levels of the injection strength k_{inj} . The NMSE values of the two tasks have almost the same variation tendency, which is associated with the underlying dynamics of the reservoir as illustrated in the bifurcation diagrams in Fig. 3. Although larger NMSE values are obtained for the parallel tasks processing, the evolution of the NMSE curves is consistent with the single

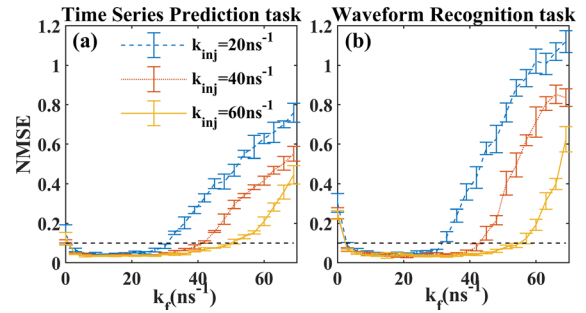


Fig. 10 The NMSE values for T-task and W-task as a function of the feedback strength k_f with $\Delta f = -20 \text{ GHz}$ and with three different values of $k_{inj} = 20, 40, \text{ and } 60 \text{ ns}^{-1}$

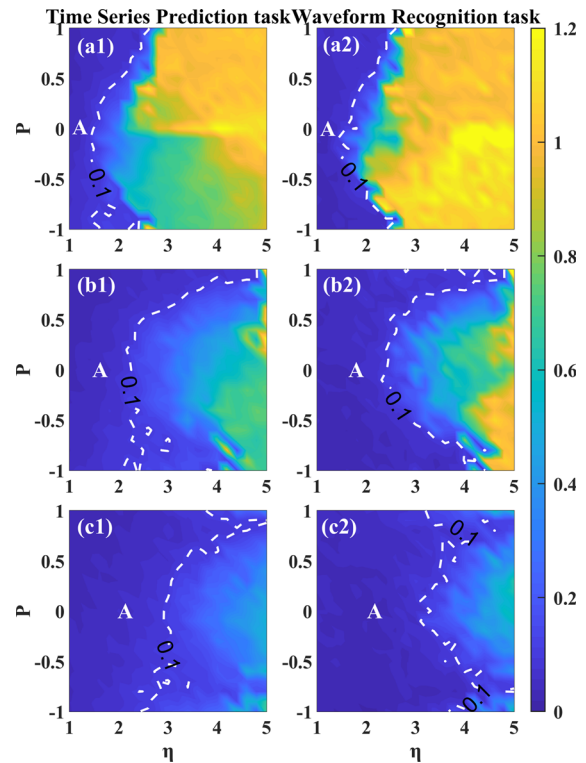


Fig. 11 Two dimensional maps of the NMSE in the plane of the pump polarization ellipticity P and the total normalized pump power η for T-task (left column) and W-task (right column) with $k_f = 30 \text{ ns}^{-1}$ and $\Delta f = -20 \text{ GHz}$. (a1, a2) $k_{inj} = 20 \text{ ns}^{-1}$, (b1, b2) $k_{inj} = 40 \text{ ns}^{-1}$, and (c1, c2) $k_{inj} = 60 \text{ ns}^{-1}$

task processing. It seems that the NMSE values for the waveform recognition task increase more dramatically than those for the time series prediction task after the reservoir enters into the nonlinear dynamics region.

Figure 11 shows the evolution of the NMSE values in the parameter space of P and η when process-

ing the T-task and W-task in parallel. For both tasks, the good performance region is depicted as A, corresponding to $NMSE \leq 0.1$. As shown in Fig. 11a1 and (a2) for $k_{inj} = 20 \text{ ns}^{-1}$, the better performance mainly appears in a narrow region A that lies on the left side of the subfigure. To achieve the excellent parallel tasks processing, the optical pumping parameters should be controlled within the overlapped range of the region A of the two tasks, occupied in the area of low η . For T-task, the region A shown in Fig. 11a1 is not symmetric about the line $P = 0$, which is different from the single tasking processing. We speculate that the change of P results in a variation of output intensities for LCP and RCP, and meanwhile the weak intensities influence the variety of virtual node states. However, Fig. 11a2 shows a good performance region for the W-task wider than the counterpart for T-task, which signifies that the W-task is less affected by the pump polarization ellipticity P . For even higher injection strengths such as $k_{inj} = 40 \text{ ns}^{-1}$ and $k_{inj} = 60 \text{ ns}^{-1}$ in Fig. 11b and c, the region A resembles the similar shape to that for $k_{inj} = 20 \text{ ns}^{-1}$ but expands to a larger area reaching to higher η . This phenomenon is also similar to the case of single task processing as displayed in Fig. 5; however, worse computing performance is obtained for the parallel tasks processing as expected.

To provide a more complete picture of the parameter dependence of the computing performance for parallel tasks processing, the NMSE values as a function of the variation of internal parameters for different k_{inj} are displayed in Figs. 12 and 13. All the conditions are the same as those in the single task processing in Fig. 6, except that the LCP and RCP modes deal with two different tasks here, respectively.

Among the internal parameters, the linear birefringence γ_p can be skillfully controlled in an optically pumped spin-VCSEL, for example, by the mechanically applied in-plane anisotropic strain [47], so its influence on the computing performance is first studied. Fig. 12a1 and a2 show the parallel processing abilities for varied γ_p . It can be seen that the computing performance for both T-task and W-task worsens when γ_p is gradually increased. The range of γ_p corresponding to $NMSE \leq 0.1$ gets wider when a larger k_{inj} is applied, similar to the single task processing case (Fig. 6a). We would like to point out that, by comparing the calculated results of the two tasks, one can find that the NMSE results of T-task are more easily to get worse than that of W-task. That is to say, the T-

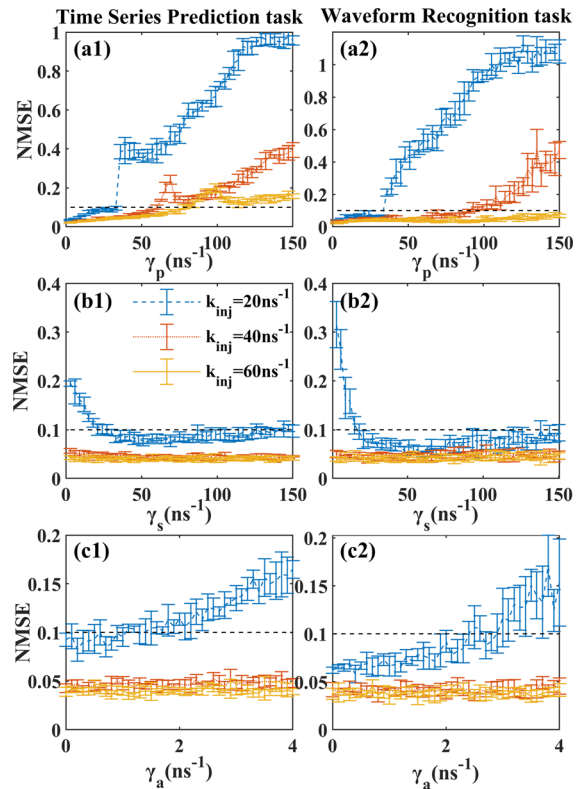


Fig. 12 The NMSE values of T-task and W-task as a function of the internal parameters for three different values of $k_{inj} = 20, 40, \text{ and } 60 \text{ ns}^{-1}$. **a** γ_p , **b** γ_s , and **c** γ_a

task is more sensitive to the variation of γ_p . Figure 12b and c show the NMSE values of the two tasks as a function of γ_s and γ_a in different injection conditions, respectively. Both parameter dependences show similar tendency under stronger injection levels of 40 ns^{-1} and 60 ns^{-1} . In this case, our RC system can maintain good parallel processing capability as γ_s or γ_a is varied, where the NMSE curves are almost unchanged and kept well below 0.1. For relatively low injection ($k_{inj} = 20 \text{ ns}^{-1}$), as γ_s is gradually increased, the NMSE is decreased from a large value and then saturated at a value close to 0.1 (good performance) for both tasks. This indicates that a large value of γ_s is beneficial for the computing task, which is important since γ_s is usually large at room temperature for most materials [45]. In contrast, for such low injection, the NMSE is monotonically increased with increasing γ_a . Especially for T-task, only a small range of γ_s can guarantee good performance, i.e., $NMSE \leq 0.1$.

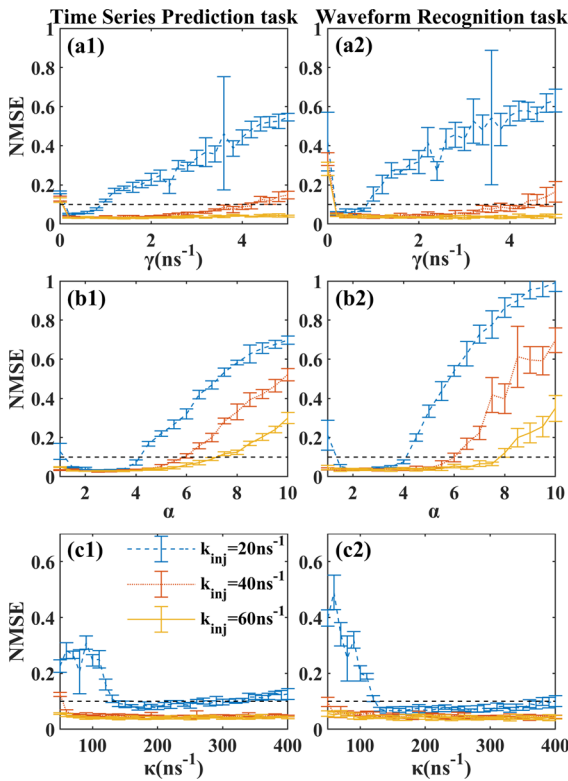


Fig. 13 The NMSE values of T-task and W-task as a function of the internal parameters for three different values of $k_{inj} = 20, 40,$ and 60 ns^{-1} . **a** γ **b** α , and **c** κ

Figures 13a1 and a2 show the NMSE values for T-task and W-task when γ is changed, respectively. The variations of parallel processing performance are mainly similar to those for single task processing. With large values of the injection strength k_{inj} , low NMSE can be achieved in a wider range of γ . The influence of the linewidth enhancement factor α on the computing performance is presented in Fig. 13b. The results for the two tasks are also similar to those for single task processing, that is, the NMSE value decreases before reaching its minimum, maintains at the lowest value for a certain range of α , and then increases with increasing α . Fig. 13c deals with the influence of the optical field decay rate κ . As shown in Fig. 13c1, for $k_{inj} = 20 \text{ ns}^{-1}$, it is difficult to achieve the desired NMSE value of below 0.1 in the case of T-task. On the contrary, in the case of W-task, one can realize good classification performance for large enough κ . For strong injection, both tasks are insensitive to the change of κ . However, for single task processing, good computing performance is

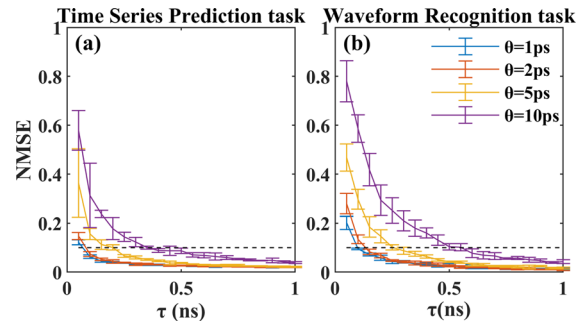


Fig. 14 The NMSE values as a function of the delay time τ with different virtual node interval θ for **a** T-task and **b** W-task

assured for the considered range of κ , independent of the injection condition.

The RC systems reported previously with parallel processing abilities only supported the information processing rate of 1 Gbps or less, since the value of the feedback delay time was limited to a nanosecond or higher [19, 24]. However, parallel executing two tasks at a high information processing rate is obviously attractive. The NMSE values as functions of the feedback delay time τ for different virtual node intervals θ are presented in Fig. 14. Different from the single task processing, the case of $\theta = 50 \text{ ps}$ is not considered since it is difficult to achieve low NMSE values here. For all considered θ , the NMSE curves show a rising trend with the decrement of τ because of the number reduction of the virtual nodes. However, it is expected that a smaller θ is more beneficial to obtaining better performance for both tasks, consistent with the single task processing. More precisely, the NMSE values of the two tasks are still less than 0.1 for an extremely short delay time ($\tau = 0.1 \text{ ns}$) when $\theta = 1 \text{ ps}$. Hence, 10 Gbps parallel tasks processing by the RC system based on an optically pumped spin VCSEL is successfully achieved.

Finally, for intuitively expound the effects of the delay time and the virtual node interval, the NMSE values versus the feedback strength for $k_{inj} = 60 \text{ ns}^{-1}$ are shown in Fig. 15. Again, for large delay times, one can still achieve desired performance for both tasks for large enough θ , i.e., $\theta = 10 \text{ ps}$. However, only the condition corresponding to $\theta = 1 \text{ ps}$ can realize parallel processing with $\text{NMSE} \leq 0.1$ when $\tau = 0.1 \text{ ns}$, as shown in Fig. 15d, in accordance with the results illustrated in Fig. 14.

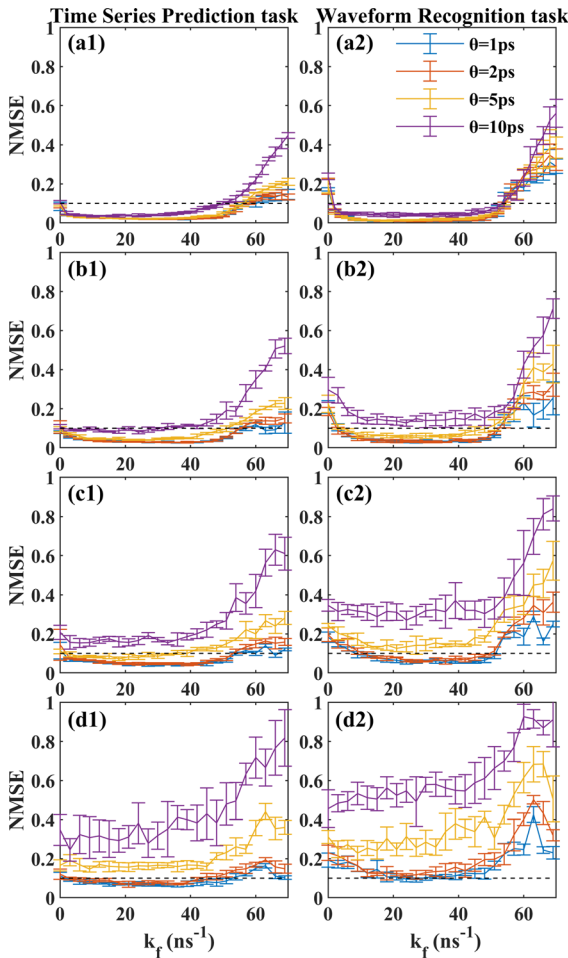


Fig. 15 The NMSE values of (a1–d1) T-task and (a2–d2) W-task as a function of the feedback strength k_f with different virtual node interval θ for **a** $\tau = 1$ ns, **b** $\tau = 0.4$ ns, **c** $\tau = 0.2$ ns, and **d** $\tau = 0.1$ ns

According to our above results, the proposed RC system based on a spin-VCSEL has the following characteristics and advantages. The spin-VCSEL provides additional pump polarization ellipticity P and can make the RC system to obtain desirable performance in a larger range of the total normalized pump power η compared to the case of an ordinary VCSEL ($P = 0$); By using the controllable LCP and RCP modes, multiple tasks processing can be realized in this RC; a smaller virtual node interval is available in the RC system due to the fast dynamics in spin-VCSEL, thus the information processing rate can be heightened for both single task processing and parallel tasks processing. Such a RC system has great application

potential in different fields, such as communication, image recognition, speech recognition and reconstructing chaotic systems [49–54]. For recovering distorted signals after transmission in ultrafast fiber communication field, the faster information processing in the spin-VCSEL-based RC system may allow for higher data encoding rates as well as longer transmission distance. For modulation format identification of optical signals, the proposed RC's multi-channel parallel processing is attractive to identify more than one signals at the same time. In addition, shorter node interval also means that the time-delayed RC system has more virtual nodes in a given delay time, which is almost necessary to ensure the classification performance in complex tasks of recognition field.

4 Conclusion

We numerically investigate the possibility to establish a time-delayed RC based on the optically pumped spin VCSEL subject to feedback and injection. A Santa Fe time series prediction task and a waveform recognition task are employed to evaluate the prediction and classification abilities of the RC system. The good performance of single task processing similar to those obtained from other conventional SL-based RC systems can be acquired by our scheme. However, when compared to the conventional RC schemes, desirable computing performance can be obtained in much wider ranges of experimentally accessible parameters in the proposed RC due to the feasible tunability of the pump intensity and polarization. We also realize multiple tasks processing using the LCP and RCP modes in the proposed RC. The consistency between the RC computing performance and the laser dynamics is discussed as well. In particular, we comprehensively study the effects of internal and external parameters on the computing performance for both single task and parallel tasks processing, and meanwhile we find that the robustness of the system to internal parameters can be effectively improved by increasing the injection strength. Moreover, the information processing rate of our RC system for executing single task and parallel tasks is improved to 20 Gbps and 10 Gbps, respectively. Our proposed RC system has the potential to develop highly integrated neuromorphic photonic systems and provide theoretical guidelines for high-speed laser-based RC systems.

Acknowledgements Yigong Yang and Pei Zhou are co-first authors. This work is supported in part by the National Natural Science Foundation of China under Grants 62004135, and 62001317, in part by the Natural Science Research Project of Jiangsu Higher Education Institutions under Grant 20KJA416001, and 20KJB510011, in part by the Natural Science Foundation of Jiangsu Province under Grant BK20200855, in part by Open Fund of IPOC (BUPT) under Grant IPOC2020-A012, in part by State Key Laboratory of Advanced Optical Communication Systems Networks, China under Grant 2021GZKF003, in part by the Startup Funding of Soochow University under Grant Q415900119.

Data availability The datasets generated during and/or analyzed during the current study are available from the corresponding author on reasonable request.

Declarations

Conflict of interest The authors declare that they have no conflict of interest.

References

- Caulfield, H., Dolev, S.: Why future supercomputing requires optics. *Nat. Photon.* **4**, 261–263 (2010)
- Woods, D., Naughton, T.: Photonic neural networks. *Nat. Phys.* **8**, 257–259 (2012)
- Hinton, G., Deng, L., Yu, D., Dahl, G.E., Mohamed, A., Jaitly, N., Senior, A., Vanhoucke, V., Nguyen, P., Sainath, T.N., Kingsbury, B.: Deep neural networks for acoustic modeling in speech recognition: the shared views of four research groups. *IEEE Signal Process. Mag.* **29**(6), 82–97 (2012)
- Steil, J.J.: Backpropagation-decorrelation: Online recurrent learning with $O(N)$ complexity. 2004 IEEE international joint conference on neural networks 2, pp 843–848 (2004)
- Verstraeten, D., Schrauwen, B., D’Haene, M., Stroobandt, D.: An experimental unification of reservoir computing methods. *Neural Networks* **20**(3), 391–403 (2007)
- Maass, W., Natschläger, T., Markram, H.: Real-time computing without stable states: a new framework for neural computation based on perturbations. *Neural Comput.* **14**(11), 2531–2560 (2002)
- Jaeger, H., Haas, H.: Harnessing nonlinearity: predicting chaotic systems and saving energy in wireless communication. *Science* **304**(5667), 78–80 (2004)
- Verstraeten, D., Schrauwen, B., Stroobandt, D., Van Campenhout, J.: Isolated word recognition with the liquid state machine: a case study. *Inf. Process. Lett.* **95**(6), 521–528 (2005)
- Verstraeten, D., Schrauwen, B., Stroobandt, D.: Reservoir-based techniques for speech recognition. The 2006 IEEE international joint conference on neural networks. 1050–1053 (2006)
- Lukoševičius, M., Jaeger, H., Schrauwen, B.: Reservoir computing trends. *Künstl. Intell.* **26**, 365–371 (2012)
- Tanaka, G., Yamane, T., Héroux, J., Nakane, R., Kanazawa, N., Takeda, S., Numata, H., Nakano, D., Hirose, A.: Recent advances in physical reservoir computing: a review. *Neural Networks* **115**, 100–123 (2019)
- Appeltant, L., Soriano, M., Van der Sande, G., Danckaert, J., Massar, S., Dambre, J., Schrauwen, B., Mirasso, C.R., Fischer, I.: Information processing using a single dynamical node as complex system. *Nat. Commun.* **2**, 468 (2011)
- Brunner, D., Soriano, M.C., Mirasso, C.R., Fischer, I.: Parallel photonic information processing at gigabyte per second data rates using transient states. *Nat. Commun.* **4**, 1364 (2013)
- Nakayama, J., Kanno, K., Uchida, A.: Laser dynamical reservoir computing with consistency: an approach of a chaos mask signal. *Opt. Express* **24**(8), 8679–8692 (2016)
- Kuriki, Y., Nakayama, J., Takano, K., Uchida, A.: Impact of input mask signals on delay-based photonic reservoir computing with semiconductor lasers. *Opt. Express* **26**(5), 5777–5788 (2018)
- Nguimdo, R.M., Erneux, T.: Enhanced performances of a photonic reservoir computer based on a single delayed quantum cascade laser. *Opt. Lett.* **44**(1), 49–52 (2019)
- Hou, Y., Xia, G., Yang, W., Wang, D., Jayaprasath, E., Jiang, Z., Hu, C., Wu, Z.: Prediction performance of reservoir computing system based on a semiconductor laser subject to double optical feedback and optical injection. *Opt. Express* **26**(8), 10211–10219 (2018)
- Guo, X., Xiang, S., Zhang, Y., Lin, L., Wen, A., Hao, Y.: High-speed neuromorphic reservoir computing based on a semiconductor nanolaser with optical feedback under electrical modulation. *IEEE J. Sel. Topics Quantum Electron.* **26**(5), 1–7 (2020)
- Nguimdo, R.M., Verschaffelt, G., Danckaert, J., Van der Sande, G.: Simultaneous computation of two independent tasks using reservoir computing based on a single photonic nonlinear node with optical feedback. *IEEE Trans. Neural Networks Learn. Syst.* **26**(12), 3301–3307 (2015)
- Nguimdo, R.M., Verschaffelt, G., Danckaert, J., Van der Sande, G.: Reducing the phase sensitivity of laser-based optical reservoir computing systems. *Opt. Express* **24**(2), 1238–1252 (2016)
- Vatin, J., Rontani, D., Sciamanna, M.: Enhanced performance of a reservoir computer using polarization dynamics in VCSELs. *Opt. Lett.* **43**(18), 4497–4500 (2018)
- Vatin, J., Rontani, D., Sciamanna, M.: Experimental reservoir computing using VCSEL polarization dynamics. *Opt. Express* **27**(13), 18579–18584 (2019)
- Guo, X., Xiang, S., Zhang, Y., Lin, L., Wen, A., Hao, Y.: Four-channels reservoir computing based on polarization dynamics in mutually coupled VCSELs system. *Opt. Express* **27**(16), 23293–23306 (2019)
- Guo, X., Xiang, S., Zhang, Y., Lin, L., Wen, A., Hao, Y.: Polarization multiplexing reservoir computing based on a VCSEL with polarized optical feedback. *IEEE J. Sel. Top. Quantum Electron.* **26**(1), 1–9 (2020)
- Vatin, J., Rontani, D., Sciamanna, M.: Experimental realization of dual task processing with a photonic reservoir computer. *APL Photon.* **5**(8), 086105 (2020)
- Nguimdo, R.M., Lacot, E., Jacquin, O., Hugon, O., Van der Sande, G., Guillet de Chatellus, H.: Prediction performance of reservoir computing systems based on a diode-pumped erbium-doped microchip laser subject to optical feedback. *Opt. Lett.* **42**(3), 375–378 (2017)

27. Takano, K., Sugano, C., Inubushi, M., Yoshimura, K., Sunada, S., Kanno, K., Uchida, A.: Compact reservoir computing with a photonic integrated circuit. *Opt. Express* **26**(22), 29424–29439 (2018)
28. Sugano, C., Kanno, K., Uchida, A.: Reservoir computing using multiple lasers with feedback on a photonic integrated circuit. *IEEE J. Sel. Top. Quantum Electron.* **26**(1), 1–9 (2020)
29. Nguimdo, R.M., Verschaffelt, G., Danckaert, J., Van der Sande, G.: Fast photonic information processing using semiconductor lasers with delayed optical feedback: role of phase dynamics. *Opt. Express* **22**(7), 8672–8686 (2014)
30. Hovel, S., Gerhardt, N., Hofmann, M., Yang, J., Reuter, D., Wieck, A.: Spin controlled optically pumped vertical cavity surface emitting laser. *Electron. Lett.* **41**(5), 251–253 (2005)
31. Hövel, S., Bischoff, A., Gerhardt, N.C., Hofmann, M.R.: Optical spin manipulation of electrically pumped vertical-cavity surface-emitting lasers. *Appl. Phys. Lett.* **92**(4), 041118 (2008)
32. Saha, D., Basu, D., Bhattacharya, P.: High-frequency dynamics of spin-polarized carriers and photons in a laser. *Phys. Rev. B* **82**(20), 205309 (2010)
33. Holub, M., Shin, J., Saha, D.: Electrical spin injection and threshold reduction in a semiconductor laser. *Phys. Rev. Lett.* **98**(14), 146603 (2007)
34. Lindemann, M., Xu, G., Pusch, T., Michalzik, R., Hofmann, M.R., Zutic, I., Gerhardt, N.C.: Ultrafast spin-lasers. *Nature* **568**, 212–215 (2019)
35. Li, N., Alexandropoulos, D., Susanto, H., Henning, I., Adams, M.: Stability analysis of quantum-dot spin-VCSELs. *Electronics* **5**(4), 83 (2016)
36. Torre, M., Susanto, H., Li, N., Schires, K., Salvade, M.F., Henning, I.D., Adams, M.J., Hurtado, A.: High frequency continuous birefringence oscillations in spin-polarized vertical-cavity surface-emitting lasers. *Opt. Lett.* **42**(8), 1628–1631 (2017)
37. Li, N., Susanto, H., Cemlyn, B., Henning, I., Adams, M.: Stability and bifurcation analysis of spin-polarized vertical-cavity surface-emitting lasers. *Phys. Rev. A* **96**(1), 013840 (2017)
38. Li, N., Susanto, H., Cemlyn, B., Henning, I., Adams, M.: Secure communication systems based on chaos in optically-pumped spin-VCSELs. *Opt. Lett.* **42**(17), 3494–3497 (2017)
39. Li, N., Susanto, H., Cemlyn, B., Henning, I., Adams, M.: Mapping bifurcation structure and parameter dependence in quantum dot spin-VCSELs. *Opt. Express* **26**(11), 14636–14649 (2018)
40. Adams, M., Li, N., Cemlyn, B., Susanto, H., Henning, I.: Algebraic expressions for the polarisation response of spin-VCSELs. *Semicond. Sci. Technol.* **33**(6), 064002 (2018)
41. Huang, Y., Zhou, P., Li, N.: High-speed secure key distribution based on chaos synchronization in optically pumped QD spin-polarized VCSELs. *Opt. Express* **29**(13), 19675–19689 (2021)
42. Huang, Y., Zhou, P., Li, N.: Broad tunable photonic microwave generation in an optically pumped spin-VCSEL with optical feedback stabilization. *Opt. Lett.* **46**(13), 3147–3150 (2021)
43. Schires, K., Seyab, R.A., Hurtado, A., Korpjarvi, V., Guina, M., Henning, I.D., Adams, M.J.: Optically-pumped dilute nitride spin-VCSEL. *Opt. Express* **20**(4), 3550–3555 (2012)
44. Susanto, H., Schires, K., Adams, M.J., Henning, I.D.: Spin-flip model of spin-polarized vertical-cavity surface-emitting lasers: asymptotic analysis, numerics, and experiments. *Phys. Rev. A* **92**(6), 063838 (2015)
45. Gahl, A., Balle, S., San Miguel, M.: Polarization dynamics of optically pumped VCSELs. *IEEE J. Quantum Electron.* **35**(3), 342–351 (1999)
46. Weigend, A.S., Gershenfeld, N.A.: Time series prediction: forecasting the future and understanding the past. 1993. <http://www-psych.stanford.edu/andreas/Time-Series/SantaFe.html>
47. Lindemann, M., Pusch, T., Michalzik, R., Gerhardt, N.C., Hofmann, M.R.: Frequency tuning of polarization oscillations: toward high-speed spin-lasers. *Appl. Phys. Lett.* **108**(4), 042404 (2016)
48. Zhang, L., Ji, J.C.: One-to-three resonant Hopf bifurcations of a maglev system. *Nonlinear Dyn.* **93**, 1277–1286 (2018)
49. Argyris, A., Bueno, J., Fischer, I.: Photonic machine learning implementation for signal recovery in optical communications. *Sci. Rep.* **8**(1), 8487 (2018)
50. Argyris, A., Bueno, J., Fischer, I.: PAM-4 transmission at 1550 nm using photonic reservoir computing post-processing. *IEEE Access* **7**, 37017–37025 (2019)
51. Cai, Q., Guo, Y., Li, P., Bogris, A., Alan Shore, K., Zhang, Y., Wang, Y.: Modulation format identification in fiber communications using single dynamical node-based photonic reservoir computing. *Photon. Res.* **9**, B1–B8 (2021)
52. Antonik, P., Marsal, N., Rontani, D.: Large-scale spatiotemporal photonic reservoir computer for image classification. *IEEE J. Sel. Topics Quantum Electron.* **26**(1), 1–12 (2020)
53. Larger, L., Baylón-Fuentes, A., Martinenghi, R., Udaltsov, V.S., Chembo, Y.K., Jacquot, M.: High-speed photonic reservoir computing using a time-delay-based architecture: million words per second classification. *Phys. Rev. X* **7**, 011015 (2017)
54. Pathak, J., Lu, Z., Hunt, B., Girvan, M., Ott, E.: Using machine learning to replicate chaotic attractors and calculate Lyapunov exponents from data. *Chaos* **27**, 121102 (2017)

Publisher's Note Springer Nature remains neutral with regard to jurisdictional claims in published maps and institutional affiliations.